Growth and nonlinear response of driven water bells

John M. Kolinski,[1] Hillel Aharoni,[1,2] Jay Fineberg,[1] and Eran Sharon[1]

[1]*Department of Physics, The Hebrew University of Jerusalem, Jerusalem 91904, Israel*

[2]*Department of Physics, University of Pennsylvania, Philadelphia, Pennsylvania 19104, USA*

A water bell forms when a fluid jet impacts upon a target and separates into a two-dimensional sheet. Depending on the angle of separation from the target, the sheet can curve into a variety of different geometries. We show analytically that harmonic perturbations of water bells have linear wave solutions with geometry-dependent growth. We test the predictions of this model experimentally with a custom target system, and observe growth in agreement with the model below a critical forcing amplitude. Once the critical forcing amplitude is exceeded, a nonlinear transcritical bifurcation occurs; the response amplitude increases linearly with increasing forcing amplitude, albeit with a fundamentally different spatial form, and distinct nodes appear in the amplitude envelope.

When a jet of fluid strikes a target with sufficient velocity, it separates from the target and forms a smooth two-dimensional sheet of fluid in the shape of a bell. Such fluid structures punctuate our daily experience, from sprinklers in the garden to sophisticated systems for heat transfer and fuel injection. Water bells adopt a rich variety of geometries at a steady state, when surface tension and fluid inertia are balanced. The bell shape depends on the angle of separation from the target, the liquid rheology, and the fluid injection conditions [1–7]. Studied in detail for flat sheets, these two-dimensional fluid structures also admit wave solutions with remarkably rich dynamics, including growth [8,9] and instability [5,10–13]. While geometry plays a dominant role in the physics governing thin elastic sheets [14–16], the effect of geometry on the dynamics of driven curved water sheets remains unexplored; even the linearized regime remains elusive [17]. Here, we first present a linearized model for the wave dynamics of a driven curved water bell, and experimentally verify its predictions for sufficiently weak forcing. We then show that the water bells undergo a distinct bifurcation to nonlinear structures, whose nodal character had previously been (mistakenly) interpreted to be due to linear waves.

We perturb the fluid sheet in our experiments by temporally varying the separation angle Ψ about its mean value at steady state Ψ_0. We do this by adjusting the height δ of a collar surrounding the jet's cylindrical flat target [Fig. 1(a)]. The brass cylinder and collar have a gap of less than 100 μm. Adjusting δ results in a linear change of Ψ in the low forcing-frequency limit [6]. With this target structure, we drive Ψ in time, $\Psi(t) = \Psi_0 + C\delta(t) = \Psi_0 + \Delta\Psi(t)$, and probe the dynamic response of the sheet. Here, $C = 0.23°/\mu$m is the constant of proportionality between Ψ_0 and δ.

We control $\Delta\Psi(t)$ by driving δ with either an electromagnetic shaker [18] or a long-throw piezoelectric linear actuator [19] that provide an angular precision of 90 arcsec. The water jet velocity u is set by air pressure applied to a variable-volume fluid reservoir; in all experiments, $u = 4.1$ m/s unless otherwise specified. Once the bell is formed, we image its silhouette with a fast camera recording at 1–5 kHz, with an exposure time of less than 100 μs to ensure an accurate detection of the bell's edge. Images recorded in this fashion for steady-state bells with different separation angles are shown in Fig. 1(a) (left). Ψ_0 is set by controlling the initial offset of δ before the excitation is applied. The sheet responds to $\Delta\Psi(t)$ by forming waves along its surface, as shown in Fig. 1(a) (right panel). We determine the wave amplitude normal to the average surface by comparing the instantaneous shape to the average background shape [Fig. 1(b)]. At our excitation frequencies (100–1000 Hz) the spatial wavelength of the response of the system varies between 1 and 10 mm with amplitudes of approximately 100 μm; therefore, the long-wavelength approximation is satisfied. A typical example of the resulting amplitude is shown in Fig. 1(c). We mitigate the effects
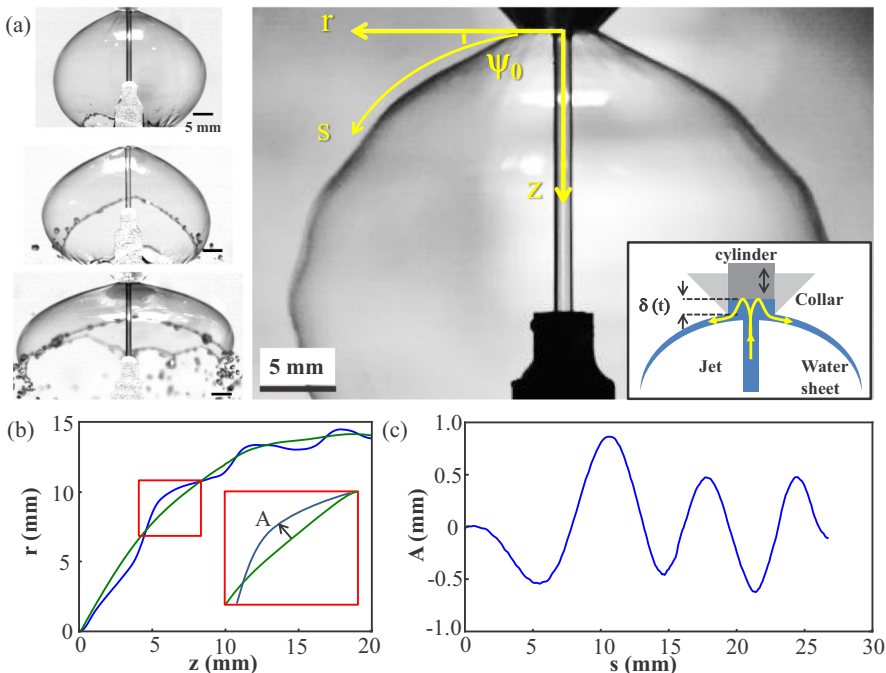
FIG. 1. Water bell shapes and amplitude measurement. (a) The steady-state bell shape is determined by the fluid velocity u (typically 4–6 m/s) and separation angle Ψ_0. Examples at left: from top to bottom, $\Psi_0 = 27°$, $21°$, and $15°$. Our two-component target geometry is shown schematically in the inset; this redirects the fluid flow to control $\Psi(t)$. When Ψ is forced periodically, waves propagate through the bell, as shown on the right. (b) The bell silhouette is determined by edge detection applied to the image. Amplitudes of the perturbed bell (blue) were measured normal to the time-averaged profile, as depicted by the arrow in the inset. (c) The amplitude is plotted as a function of the arclength s of the background profile.

of gravity by using a small 1 mm diam jet with a high flow rate; water bell shapes were identical for jets aligned both along and perpendicular to gravity. All of our experiments were in the smooth-sheet regime [12], where the sheet is stable to shear instabilities [10].

The steady-state shape of the water bell is set by a balance of fluid inertia and surface tension [1,7]; this balance can be written in terms of the mean curvature H as

$$4\gamma H = \rho h a, \tag{1}$$

where γ is the surface tension, ρ is the fluid density, h is the sheet thickness, and a is the centripetal acceleration. Analysis yields a length scale $L = \frac{Wu}{4\pi\gamma}$, which sets the radial extent of a water bell for finite separation angles, where W is the mass flux. The fluid velocity u is constant throughout the bell when perturbations are small [20]. Using the length L and time L/u scales we form dimensionless variables, e.g., radius $\tilde{r} = r/L$ or frequency $\tilde{f} = fL/u$.

Antisymmetric modes [8], where the water sheet deflects from its mean position but does not dilate in thickness, successfully describe the dynamics of flat water bells [9,13] in the long-wavelength $\lambda/h \gg 1$ limit. We apply a similar analysis to arbitrary bell geometries, where the curved geometry alters the profile of the sheet thickness h as a function of the arclength beyond the target s. A more detailed derivation is provided in Appendix A. We rewrite the force balance Eq. (1) in dimensionless form,

$$\left[\frac{\partial}{\partial\tilde{t}} + \frac{\partial}{\partial\tilde{s}}\right]^2 \tilde{r} - \tilde{r}\frac{\partial^2\tilde{r}}{\partial\tilde{s}^2} = \left(\frac{\partial\tilde{r}}{\partial\tilde{s}}\right)^2 - 1. \tag{2}$$

The bell's steady-state shape $r_0(s)$ can then be found by assuming time independence for fixed Ψ_0. For small perturbations around r_0, Eq. (2) can be linearized to yield the dispersion relation

$$(\tilde{\omega} - \tilde{k})^2 = \tilde{r}_0 \tilde{k}^2 - \frac{d^2 \tilde{r}_0}{d\tilde{s}^2} - 2i \frac{d\tilde{r}_0}{d\tilde{s}} \tilde{k}. \tag{3}$$

Equation (3) has two wave solutions, one propagating rapidly and one propagating slowly. The geometry-dependent imaginary terms correspond to growth or decay of the applied perturbation. Solving for the amplitude response using Eq. (3) as described in Appendix A, we can directly compare with the measured response of the water bell. We find that *all* perturbations are unstable. The growth rate is proportional to $\frac{d\tilde{r}_0}{d\tilde{s}}$ and thus depends on the bell shape. This dependence on geometry results from both the curvature of the bell and the thinning of the spreading sheet—the thinner sheet contains less mass per unit area, and thus deviates further from the mean shape, leading to the growth of a perturbation. We find that the slowly propagating mode grows *more rapidly*, and that this term dominates the response of the driven water sheet. The extent, however, to which it dominates is a strong function of geometry and forcing frequency. A similar growth mechanism arises for flat fluid sheets [8,9,12,17]. We note that in a previous analysis of flat water bells, the amplitude response is treated as either constant along the water bell [13] or empirically fitted [17]. In the high-frequency limit, where $\lambda/L < 1$, Eq. (3) prescribes mode velocities of the simple form

$$v_\pm = (1 \pm \sqrt{\tilde{r}_0})u, \tag{4}$$

where the velocity added (subtracted) from the fluid velocity is the Taylor-Culick velocity set by the local sheet thickness $v_{tc} = \sqrt{\tilde{r}_0}u = \sqrt{\frac{2\gamma}{\rho h}}$.

To test our theory with experiments, we calculate the amplitude response described by the dispersion relation Eq. (3) (see Appendix A). The measured growth is not due to the Kelvin-Helmholtz instability, as the Weber number based on the jet diameter (<300) [21] is below the threshold value (500–800) for this instability [5,22]. Our water bells are therefore in the smooth-sheet regime [12].

We measure the bell response for a variety of Ψ_0 driven over a range of different frequencies and compare the observed response with the predicted growth. We reduce the forcing amplitude, $\Delta\Psi < 0.2°$ [23], to keep the disturbance as small as possible, and therefore most consistent with the anticipated range of validity of the calculation. Examples for two very different water bell shapes are shown in Fig. 2(a). Negative (positive) values of the imaginary component of the phase $\text{Im}\{k_\pm\}$ correspond to growth (decay). In Fig. 2(b), we plot this quantity normalized by its peak value for the slow- and fast-propagating modes as a function of s along a bell driven at 80 Hz for $\Psi_0 = 37°$. Strikingly, we predict that the fast-propagating mode will *decay*, whereas the slow-propagating mode will *grow*. The results are shown in the red dashed line in Fig. 2(c). The observed water bell response (solid line) agrees well with the theoretically predicted response (dashed line) for very different water bells driven at both 80 Hz with $\Psi_0 = 19°$ and $37°$ in Fig. 2(c) and 200 Hz with $\Psi_0 = 14.7°$ and $32°$ in Fig. 2(d).

When the amplitude of the applied forcing exceeds a critical value, we observe a strikingly different amplitude response, and the agreement with the growth predicted in our linearized model abruptly breaks down. We see that a rapid growth of the bell's response only occurs *after* $\Delta\Psi$ exceeds a critical value $\Delta\Psi_c \sim 0.5°$. For $\Delta\Psi > \Delta\Psi_c$, the amplitude response grows linearly with $\Delta\Psi$, as shown in Fig. 3. As this occurs, the form of the amplitude envelope changes dramatically, as shown in Fig. 3 (inset). Beyond $\Delta\Psi_c$, the second-harmonic amplitude both appears and increases linearly with $\Delta\Psi$, as shown by the square symbols in Fig. 3. *Only* in this regime does the spatial profile of the amplitude envelope possess the clear nodal structure. We surmise that the same nonlinear behavior is at the root of the nodal structure observed previously, for the case of the forced flat water bell [13,17] in the smooth-sheet regime [12].

As the amplitudes increase, the nodes denoted in the inset of Fig. 3 become more pronounced. This pronounced nodal structure at large amplitudes indicates that the fast and slow modes contribute
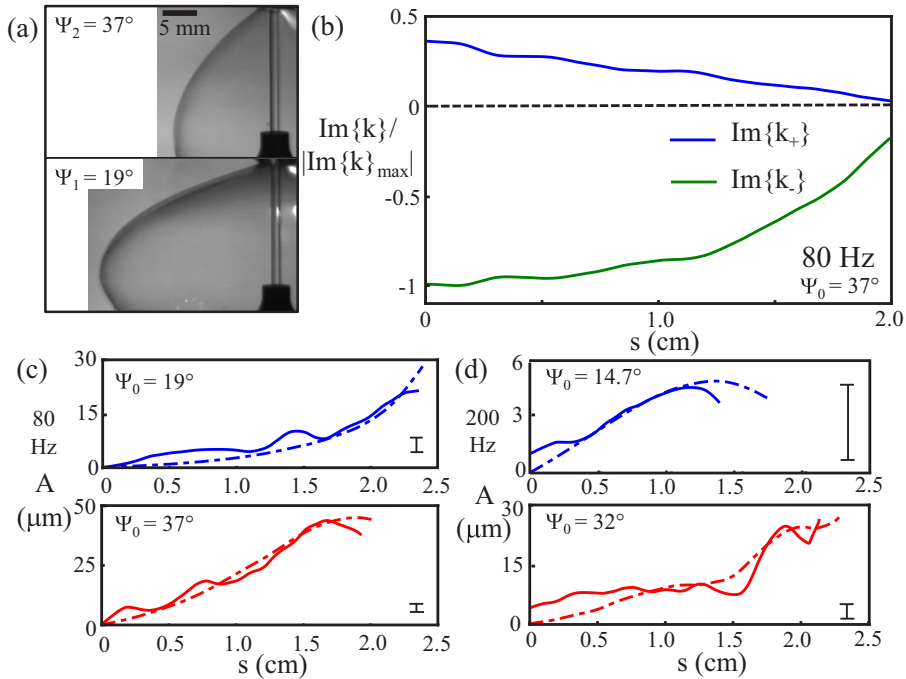
FIG. 2. Linear growth at small forcing amplitudes $\Delta\Psi < 0.3°$. (a) Two water bells with $\Psi_0 = 37°$ (top) and $19°$ (bottom). (b) The growth rate Im$\{k\}$ for a water bell driven at 80 Hz with $\Psi_0 = 37°$ is plotted as a function of arclength for the fast k_+ and slow k_- modes. Negative (positive) values of Im$\{k\}$ correspond to growth (decay). The predicted amplitudes (dashes) agree quantitatively with the experimental data (solid lines) for (c) $f = 80$ Hz and (d) 200 Hz with $\Psi_0 = 14.7°$ and $32°$. Representative error bars are included on the right of each plot. Values of A are scaled to coincide at a single point; the key spatial features of the calculations and experiment are in good agreement.

roughly equally to the response. This is in striking contrast to the unequal growth predicted by the linear theory and observed for small excitation amplitudes (Fig. 2).

In Fig. 3 we considered the behavior of the superposed nonlinear modes at a point. By separating the two modes in this regime, we can explore their spatial and temporal behavior beyond $\Delta\Psi_c$. In Fig. 4 we present space-time plots of the two separated modes within the nonlinear regime. The modes were separated via spatial filtering with a cutoff wave number $k = 2\pi f/u \approx 1.5$ mm^{-1}. The instantaneous amplitudes undergo perfect destructive interference at the nodes, as seen at $s = 5, 8$, and 10 mm in Fig. 4(b).

Up to this point we have considered the amplitude response of perturbations to the bell. Let us now consider the phase velocities of the fast and slow modes independently. Superimposed on the data in Figs. 4(c) and 4(d) are trajectories of constant phase $t_\pm$, calculated using the steady-state profiles of the bell $r_0(s)$ and the *linear* phase velocities $v_\pm$ of Eq. (4),

$$t_\pm(s) = \int_0^s \frac{ds}{v_\pm[r_0(s)]}. \tag{5}$$

Despite the clearly nonlinear amplitude response, the predicted phase trajectories perfectly correspond with our measurements in Figs. 4(c) and 4(d). This demonstrates that nonlinear frequency shifts are small, and thus the linear dispersion relation accurately describes the wave speeds beyond $\Delta\Psi_c$.

The water bell geometry, set by Ψ_0, alters the relationship between s and h (and thus v_{tc}), changing the locations where the slow and fast modes constructively and destructively interfere.
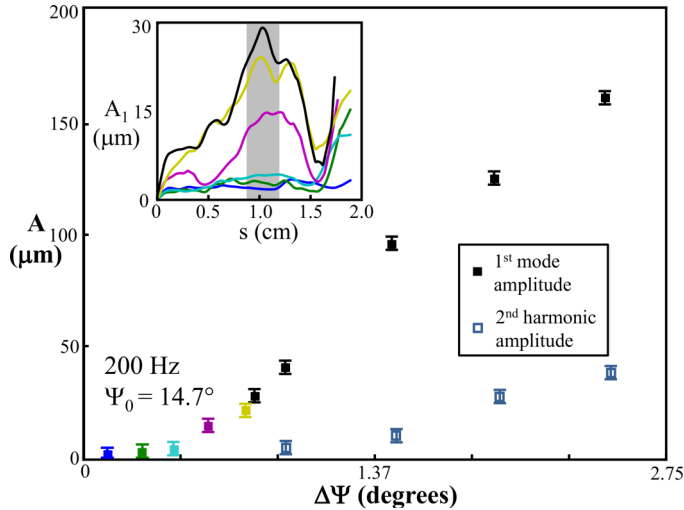
GROWTH AND NONLINEAR RESPONSE OF DRIVEN ...

FIG. 3. Departure from linear growth at forcing amplitudes $\Delta\Psi > 0.5°$. The amplitude of the bell's response as measured at the emergent antinode A_1 (indicated by the gray rectangle inset), remains small until a critical value of $\Delta\Psi_c \sim 0.5°$ is exceeded. For $\Delta\Psi > \Delta\Psi_c$, spatial features of the amplitude envelope change dramatically, and the nodal structure emerges; a node is seen at $s \sim 1.6$ cm. Here, $f = 200$ Hz and $\Psi_0 = 14.7°$. A phenomenological model of the nonlinear character of the water bell's response is developed in Appendix B. Colors in the main graph correspond to the response profiles shown in the inset; open squares denote the amplitude of the second harmonic, which grows from zero after the threshold $\Delta\Psi_c$ is exceeded. A similar bifurcation is observed at other frequencies in the high-frequency limit $\tilde{f} \gg 1$. Error bars represent typical values of the standard deviations of A_1 over the gray region plotted in the inset.

Whereas in Fig. 4 we considered a single example, in Fig. 5 we demonstrate that the linear theory quantitatively predicts nodal locations of waves within the nonlinear regime in general. To do this, we hold Ψ_0 constant as we sweep over the forcing frequency. Node locations depend on the node index n, and the water bell parameters L, u, and Ψ_0. For each Ψ_0, nodal locations are predicted to be well-defined functions of dimensionless frequencies fL/nu and distances r/L. Comparison of the predicted nodal locations with experiment (Fig. 5) shows excellent agreement. Each different value of Ψ_0 sweeps out a universal surface for the nodal location.

Our experiments and theory illuminate the dominant role of geometry in the dynamics of driven water bells. These effects are observed by geometry-dependent growth of slow and fast propagating modes in the linear regime. Surprisingly, it is the *nonlinear* saturation of the predicted growth that ultimately leads to the nodal patterns observed in driven water bells. For $\Delta\Psi > \Delta\Psi_c$, both the fast and slow modes contribute equally to the amplitude envelope with comparable amplitudes. These two nonlinear modes linearly increase with the driving, empirically locking onto one another. It is this *nonlinear locking* of the two modes that gives rise to the clear nodal structure along the bell. This is in stark contrast with the very different growth rates for these two modes that appear for $\Delta\Psi < \Delta\Psi_c$. Empirically, this nonlinear behavior does not significantly affect the dispersion relations of the fast and slow modes, as nonlinear phase shifts are small.

How do the fast and slow modes attain comparable amplitudes for $\Delta\Psi > \Delta\Psi_c$, when the linear growth of the fast mode is so much less than the growth of the slow mode? A plausible scenario is that the growth of the slow mode saturates, while the fast mode continues to rapidly grow until its amplitude becomes comparable to the amplitude of the slow mode, resulting in the observed interference pattern. The linear increase of A_1 for $\Delta\Psi > \Delta\Psi_c$ suggests a normal form for these dynamics that is dominated by a quadratic saturation term, the hallmark of a transcritical bifurcation. The phenomenological description provided in Appendix B captures all of the dominant features
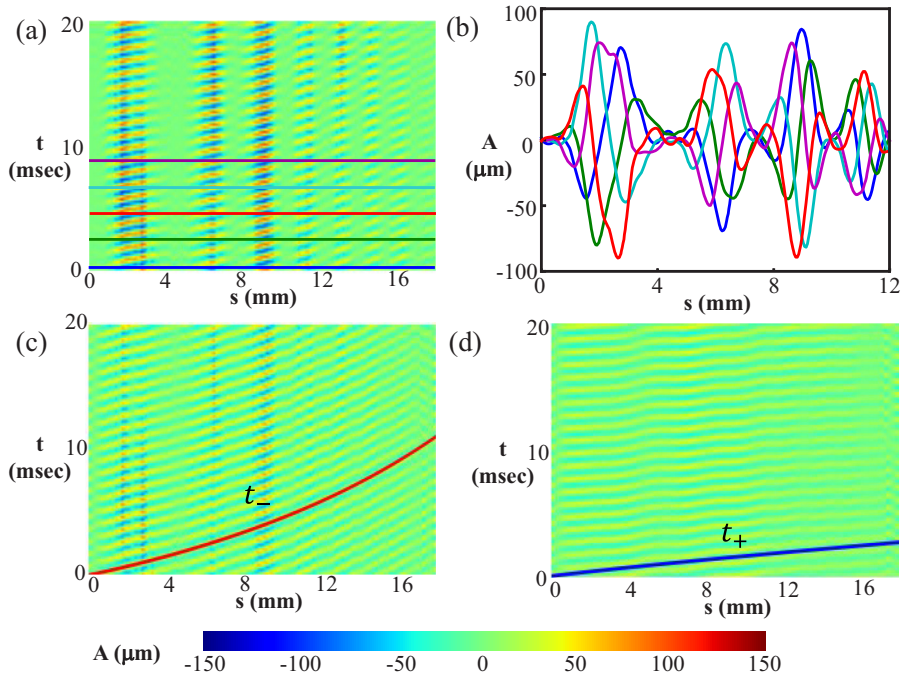
FIG. 4. Instantaneous profiles for a driven water bell ($\Delta \Psi \approx 1.4°$, $\tilde{f} \approx 7.5$). (a) The nodes in the amplitude envelope appear as faint green. (b) Instantaneous profiles as a function of s. Line colors correspond to the colored horizontal lines in (a). Well-defined nodes appear at several values of s. Separated (c) slow and (d) fast modes are obtained by spatially filtering the raw data with a cutoff frequency $k = 2\pi f/u \approx 1.5$ mm^{-1}. Modes are coupled to the bell's geometry by v_{tc}, whose local value is a function of Ψ_0. Trajectories of constant phase (lines) calculated using steady-state bell parameters agree well with measured values.
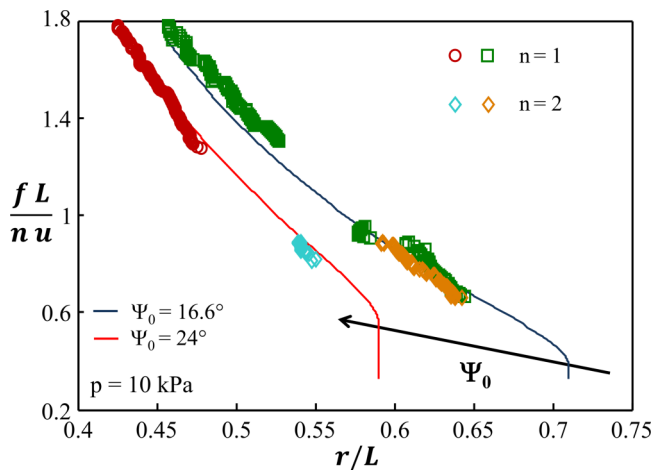

FIG. 5. Nodal structure for water bells of arbitrary geometry. (a) Nondimensional nodal locations collapse onto a single line for each value of Ψ_0; changing Ψ_0 sweeps out a nodal location surface as a function of $\tilde{f}$ and $\tilde{r}$, indicated by the arrow. Nodal locations for two bells driven over a range of frequencies are compared with predictions (solid lines) and measurements for $n = 1$ and $n = 2$ (symbols; colors indicate different n). Experimental data agree well with the predictions. Inset: Raw data of normalized amplitude and predicted nodal locations corresponding to the red curve and points in the main plot.

of the data plotted in Fig. 3. Whereas quadratic saturation is prohibited for systems with reflection symmetry, a curved water bell loses this symmetry, once perturbed about a finite separation angle; a finite negative perturbation from Ψ_0 is not equivalent to a positive one, leading to the observed linear growth of A_1 beyond the critical forcing. The development of a weakly nonlinear theoretical description of these dynamics is a logical next step in understanding this instability.

Important questions concerning the stability of the water bell for large $\Delta\Psi$ and the effects of geometry on atomization of the fluid due to bell breakdown remain open.

APPENDIX A: DEVELOPMENT OF GEOMETRY-DEPENDENT GROWTH THEORY

The equation of motion for the water bell is

$$4\gamma H = \rho h a,$$

$$2\gamma\left(\frac{r''}{\sqrt{1-r'^2}} - \frac{\sqrt{1-r'^2}}{r}\right) = \frac{W}{2\pi r u}\frac{(\partial_t + u\,\partial_s)^2 r}{\sqrt{1-r'^2}}. \tag{A1}$$

As in the main text, r is the radius of the bell, W is the mass flux of the jet, u is the velocity of the fluid, which is assumed to be constant and tangent to the water sheet, γ is surface tension, and the prime $'$ represents derivatives with respect to s, the arclength coordinate. ρ and h are the water density and the local thickness of the fluid sheet, respectively, and the equality $W = 2\pi r h \rho u$ results from mass conservation. Defining the characteristic length $L = \frac{Wu}{4\pi\gamma}$ and the nondimensional variables $\tilde{r} = \frac{r}{L}, \tilde{s} = \frac{s}{L}, \tilde{t} = \frac{ut}{L}$, yields our Eq. (2),

$$\left[\frac{\partial}{\partial\tilde{t}} + \frac{\partial}{\partial\tilde{s}}\right]^2 \tilde{r} - \tilde{r}\frac{\partial^2\tilde{r}}{\partial\tilde{s}^2} = \left(\frac{\partial\tilde{r}}{\partial\tilde{s}}\right)^2 - 1. \tag{A2}$$

To find the steady-state shape of the bell we set the time derivatives $\frac{\partial}{\partial\tilde{t}}$ to zero; then assuming $r(0) = 0$ and $r'(0) = \cos\Psi_0$, we get

$$\tilde{r}_0(\tilde{s}) = 1 - \sqrt{1 + \tilde{s}^2 - 2\tilde{s}\cos\Psi_0}. \tag{A3}$$

Perturbing Eq. (A2) around the steady-state solution (A3), i.e., substituting $\tilde{r}(\tilde{s},\tilde{t}) = \tilde{r}_0(\tilde{s}) + \delta(\tilde{s},\tilde{t})$ into Eq. (A2), yields

$$\left[\frac{\partial}{\partial\tilde{t}} + \frac{\partial}{\partial\tilde{s}}\right]^2 \delta = \tilde{r}_0\delta'' + \tilde{r}_0''\delta + 2\tilde{r}_0'\delta' + \delta\delta'' + \delta'^2. \tag{A4}$$

When considering only small perturbations, one can keep only linear terms in δ to get

$$\left[\frac{\partial}{\partial\tilde{t}} + \frac{\partial}{\partial\tilde{s}}\right]^2 \delta = \tilde{r}_0\delta'' + \tilde{r}_0''\delta + 2\tilde{r}_0'\delta', \tag{A5}$$

which after a Fourier transform becomes our Eq. (4), the dispersion relation for small perturbations,

$$(\tilde{\omega} - \tilde{k})^2 = \tilde{r}_0\tilde{k}^2 - \tilde{r}_0'' - 2i\tilde{r}_0'\tilde{k}. \tag{A6}$$
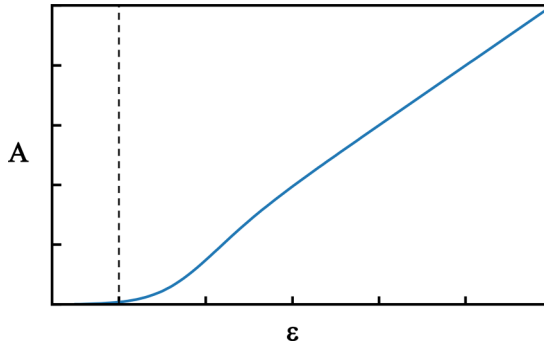
FIG. 6. The response A as described by the phenomenological model in Eq. (B1) is plotted as a function of ϵ. A is the generalized response, representing distance from the linear solution at a fixed value of t (s in our experiment). ϵ represents the distance from the critical forcing from our experiments, $(\Delta\Psi - \Delta\Psi_c)/\Delta\Psi_c$. The phenomenological model captures all the key features observed in our experimental data, both below and above $\Delta\Psi_c$, including the linear increase of A in the nonlinear regime.

In order to solve for the amplitudes of the waves, we first explicitly solve Eq. (A6) for the two local complex wave numbers $k_{\omega,\Psi_0}^{\pm}$ at every point,

$$k_{\omega,\Psi_0}^{\pm}(s) = \frac{\tilde{\omega} - i\tilde{r}_0' \pm \sqrt{\tilde{\omega}^2\tilde{r}_0 - 2i\tilde{\omega}\tilde{r}_0' + (\tilde{r}_0 - 1)\tilde{r}_0'' - \tilde{r}_0'^2}}{(1 - \tilde{r}_0)L}. \tag{A7}$$

Here, the dependence on Ψ_0 and s comes from the water bell's steady-state solution $r_0(\Psi_0, s)$ [Eq. (A3)]. In order to solve for the amplitude, we integrate the phase along the water bell as follows,

$$A_{\omega,\Psi_0}^{\pm}(s) = A^{\pm}(s_0) \exp i \int_{s_0}^{s} d\sigma k_{\omega,\Psi_0}^{\pm}(\sigma), \tag{A8}$$

where s_0 is the arclength matching the initial radius of the target, via the relation $r_0(s_0) = r_{\text{target}}$. Because the target clamps A such that $A^+(s_0) + A^-(s_0) = 0$, the total amplitude can be written for any value of s as

$$A_{\omega,\Psi_0,s_0}(s) = A_0\left(e^{i\int_{s_0}^{s} d\sigma k_{\omega,\Psi_0}^{+}(\sigma)} - e^{i\int_{s_0}^{s} d\sigma k_{\omega,\Psi_0}^{-}(\sigma)}\right). \tag{A9}$$

Equation (A9) can be integrated for an arbitrary water bell geometry in order to calculate $A(s)$.

APPENDIX B: PHENOMENOLOGICAL MODEL FOR NONLINEAR RESPONSE OF THE WATER BELL

We observe an abrupt bifurcation of the water bell's response beyond a critical forcing $\Delta\Psi_c$. In order to understand the nonlinear character of this response, we consider the following normal form. For simplicity, we consider the normal form for only a single mode,

$$\tau \frac{\partial A}{\partial t} = \epsilon A + g A^2. \tag{B1}$$

Here, A is the order parameter that represents the distance from the unstable solution, Eq. (A9), for $\epsilon > 0$. Here, the saturation term scales as A^2 due to the broken up-down symmetry; this enables the linear increase in A for $\Delta\Psi > \Delta\Psi_c$. We note that this is an equation for A as a function of t, not of s, but the two are related by $s = vt$, where v is the advective velocity of the mode. In terms of the quantities we measured, $\epsilon \sim (\Delta\Psi - \Delta\Psi_c)/\Delta\Psi_c$. Equation (B1) can be solved analytically, and its

closed form solution is

$$A(t) = \frac{A_0 A_\infty e^{\alpha t}}{A_0(e^{\alpha t} - 1) + A_\infty},\tag{B2}$$

where $A_0 = A(t = 0)$, $A_\infty = \epsilon/g$ is the saturation amplitude, and $\alpha = \epsilon/\tau$ is the growth rate of the instability.

Does this model qualitatively describe the response of the water bell observed in our experiment? In order to answer this question, we examine the behavior of A around the critical value $\epsilon = 0$, as shown in Fig. 6. Here, the generalized features of an initially slow rise, followed by a rapid rise beyond $\epsilon = 0$ and a convergence on a linear increase with ϵ, are all captured by this simple model, demonstrating qualitative similarity to the behavior observed in our experimental data, shown in Fig. 3.

Extending Eq. (B1) to include both the fast and slow modes, and a coupling term, both capture the nodal structure and reproduce the nonlinear locking mechanism described in the text.

---

[1] C. Clanet, Waterbells and liquid sheets, Annu. Rev. Fluid Mech. **39**, 469 (2007).

[2] F. Savart, Mémoire sur le choc d'une veine liquide lancée contre un plan circulaire, Ann. Chim. **54**, 56 (1833).

[3] F. Savart, Suite du mémoire sur le choc d'une veine liquide lancée contre un plan circulaire, Ann. Chim. **54**, 113 (1833).

[4] E. Villermaux, V. Pistre, and H. Lhuissier, The viscous Savart sheet, J. Fluid Mech. **730**, 607 (2013).

[5] E. Villermaux and C. Clanet, Life of a flapping liquid sheet, J. Fluid Mech. **462**, 341 (2002).

[6] C. Clanet and E. Villermaux, Life of a smooth liquid sheet, J. Fluid Mech. **462**, 307 (2002).

[7] G. Taylor and L. Howarth, The dynamics of thin sheets of fluid. I. Water bells, Proc. R. Soc. London, Ser. A **253**, 289 (1959).

[8] G. Taylor, The dynamics of thin sheets of fluid. II. Waves on fluid sheets, Proc. R. Soc. London, Ser. A **253**, 296 (1959).

[9] M. S. Tirumkudulu and M. Paramati, Stability of a moving radial liquid sheet: Time-dependent equations, Phys. Fluids **25**, 102107 (2013).

[10] H. B. Squire, Investigation of the instability of a moving liquid film, Br. J. Appl. Phys. **4**, 167 (1953).

[11] N. Dombrowski and W. R. Johns, The aerodynamic instability and disintegration of viscous liquid sheets, Chem. Eng. Sci. **18**, 203 (1963).

[12] J. C. P. Huang, The break-up of axisymmetric liquid sheets, J. Fluid Mech. **43**, 305 (1970).

[13] N. Bremond, C. Clanet, and E. Villermaux, Atomization of undulating liquid sheets, J. Fluid Mech. **585**, 421 (2007).

[14] E. Cerda and L. Mahadevan, Geometry and Physics of Wrinkling, Phys. Rev. Lett. **90**, 074302 (2003).

[15] Y. Klein, E. Efrati, and E. Sharon, Shaping of elastic sheets by prescription of non-Euclidean metrics, Science **315**, 1116 (2007).

[16] S. Armon, E. Efrati, R. Kupferman, and E. Sharon, Geometry and mechanics in the opening of chiral seed pods, Science **333**, 1726 (2011).

[17] M. Paramati, M. S. Tirumkudulu, and P. J. Schmid, Stability of a moving radial liquid sheet: Experiments, J. Fluid Mech. **770**, 398 (2015).

[18] Unholtz-Dickie model 5 PM shaker.

[19] Piezomechanic piezo stack with 80 μm stroke.

[20] The mean shape of the water bell remains unchanged during forcing. If the fluid velocity were strongly altered by the forcing, we would expect a significant shift to the mean shape; since the mean shape is unaltered, the water velocity must remain constant.

[21] For water with density $\rho = 1000$ kg/m^3, surface tension $\gamma = 0.06$, and velocity $u = 4.1$ m/s, the Weber number is We $= \frac{\rho v^2 d_j}{\gamma} \approx 250$.

[22] J. B. Keller and I. Kolodner, Instability of liquid surfaces and the formation of drops, J. Appl. Phys. **25**, 918 (1954).

[23] $\Delta\Psi = 0.2°$ corresponds to a displacement of 1 μm of the target component; displacement of the target component is verified in each experiment using a Philtec fiber-optic displacement sensor.